

Rupture Process during the M_w 8.1 2017 Chiapas Mexico Earthquake: Shallow Intraplate Normal Faulting by Slab Bending

R. Okuwaki¹, and Y. Yagi²

¹Graduate School of Life and Environmental Sciences, University of Tsukuba, 1-1-1 Ten'nodai, Tsukuba, Ibaraki 305-8572, Japan.

²Faculty of Life and Environmental Sciences, University of Tsukuba, 1-1-1 Ten'nodai, Tsukuba, Ibaraki 305-8572, Japan.

Corresponding author: Ryo Okuwaki (rokuwaki@geol.tsukuba.ac.jp)

Key Points:

- A source model of the 2017 Chiapas earthquake was constructed by kinematic waveform inversion using teleseismic P waveforms
- The model favors a shallow rupture area in the upper part of the slab centered at 28 km depth
- The rupture process was driven by down-dip extensional stresses due to slab bending and terminated at a subducting fracture zone

Abstract

A seismic source model for the M_w 8.1 2017 Chiapas, Mexico, earthquake was constructed by kinematic waveform inversion using globally observed teleseismic waveforms, suggesting that the earthquake was a normal faulting event on a steeply dipping plane, with the major slip concentrated around a relatively shallow depth of 28 km. The modeled rupture evolution showed unilateral, down-going propagation northwestward from the hypocenter, and the down-dip width of the main rupture was restricted to less than 30 km below the slab interface, suggesting that the down-dip extensional stresses due to the slab bending were the primary cause of the earthquake. The rupture front abruptly decelerated at the northwestern end of the main rupture where it intersected the subducting Tehuantepec Fracture Zone, suggesting that the fracture zone may have inhibited further rupture propagation.

Plain Language Summary

Earthquakes can be caused by normal faulting in a tensional stress field within a subducting plate, making it of critical importance to know how a plate is subducting and what type of earthquakes can be expected in a particular region. We modeled the slip history of such an event, the magnitude 8.1 Chiapas, Mexico, earthquake of September 8, 2017. Our modeling shows that normal faulting occurred mainly at a relatively shallow depth (28 km) and the width of the rupture down the dip of the subducting plate was restricted to less than 30 km. We suggest that the slab is bending around the source region and that the resulting extensional stresses were the primary force causing the 2017 Chiapas earthquake. The rupture decelerated abruptly and ceased near the subducting Tehuantepec Fracture Zone, suggesting that the fracture zone acted as a barrier against rupture propagation.

1. Introduction

Southern Mexico is a seismically active region, where the Cocos and Rivera plates are subducting northeastward beneath the North America plate at a rate of ~60 mm/yr and ~20 mm/yr, respectively (DeMets et al., 2010), and where the large earthquakes ($M > 7$) have struck at short time intervals during the past century (e.g., Pardo & Suarez, 1995; Ramírez-Herrera et al., 2011; Singh et al., 1981). The southern Mexico subduction zone (Figure 1) is noted for the frequent occurrence of the large intraplate, normal-faulting earthquakes at shallow and intermediate depths within the subducting Cocos plate (e.g., Mikumo et al., 2002; Rebollar et al., 1999b; Santoya et al., 2005; Singh et al., 1985), which can be explained by stress transfer from the preceding interplate earthquakes (Lemoine et al., 2002; Mikumo et al., 1999, 2000) and by slab unbending due to continental loading (Fujita & Kanamori, 1981).

On September 8, 2017 at 04:49:18 UTC, a large and destructive earthquake occurred along the Chiapas coast of southern Mexico. The Servicio Sismológico Nacional of the Universidad Nacional Autónoma de México (SSN UNAM) reported that the earthquake occurred offshore of the town on Pijijiapan, with a hypocenter 58 km beneath 14.85°N, 94.11°W (Figure 1). The SSN assigned it a moment magnitude of M_w 8.2, making it one of the largest instrumentally recorded earthquakes in Mexico (Ramírez-Herrera et al., 2011; Singh et al., 1981; SSN UNAM Special Report, 2017). A cross section of the source area is shown in Figure 2a, summarizing the focal depths of the centroid moment tensor (CMT) solutions fetched from database of the Japan Meteorological Agency (JMA; http://www.data.jma.go.jp/svd/eqev/data/mech/world_cmt/fig/cmt20170908044921.html), the

SCARDEC compilation (Vallée et al., 2011; Vallée and Douet, 2016; <http://scardec.projects.sismo.ipgp.fr>), the Global CMT (GCMT) project (Ekström et al., 2012; <http://www.globalcmt.org/CMTsearch.html>), the GEOFON project (<http://geofon.gfz-potsdam.de/eqinfo/list.php>), and the U.S. Geological Survey National Earthquake Information Center (<https://earthquake.usgs.gov/earthquakes/eventpage/us2000ahv0>). These solutions lie at depths of 40 to 70 km below the slab interface inferred by using the Slab1.0 model (Hayes et al., 2012), and steeply dipping ($\sim 75^\circ$) normal faults with strikes of $\sim 315^\circ$, nearly parallel to the Middle American Trench (MAT), are the common mechanism of these solutions, which indicates that the 2017 Chiapas earthquake was an intraplate normal-faulting event.

Intraplate normal faulting in a subducting plate can occur in a tensile stress field due to plate bending at shallow depths and near the trench, to slab pull from the negative buoyancy of the subducting plate, and to unbending of the subducting plate beneath a strongly coupled interface at intermediate depths beneath the continental plate (Astiz et al., 1988; Fujita & Kanamori, 1981; Isacks et al., 1968; Spence, 1986). The epicenter determined by the SSN is 55 km landwards of the trench and 115 km southwest of Pijijiapan on the coast (Figures. 1 and 2a), a position between the typical locations of large intraplate normal-faulting earthquakes, which are either near the trench or under the continent (e.g., Astiz et al., 1988). According to the thermal structural modeling of the region (Manea & Manea, 2008), at the SSN epicenter the 300° – 700° isotherms are at a depth range of 23–38 km, and the mean depth of the CMT solutions (53.1 km; Figure 2a) would be beyond the 1000°C isotherm. The variance distribution of the focal depth and the half-duration of the source time function, obtained by the CMT analysis in this study (Figure 2b and Text S1), has a minimum at 64.0 km depth, which is consistent with the other CMT solutions. However, there are two roughly equal minima, and the second is at a depth of around 20 km. There is a well-known trade-off between the focal depth and the source time function when determining the focal parameters for the shallow large earthquakes, and estimates of focal depth can be deceptive when it is difficult to distinguish the differences in synthetic waveforms (Christensen & Ruff, 1985). Moreover, the geological setting of the source region is probably complex because the Tehuantepec Fracture Zone (TFZ) on the Cocos plate is subducting near the source region (Manea et al., 2003; Manea & Manea, 2008; Menard & Fisher, 1958), and the geometry of the subducting plate differs across the TFZ (Bravo et al., 2004; LeFevre & McNally, 1985; Ponce et al., 1992; Rebollar et al., 1999a). Thus, a detailed analysis of the rupture process of the 2017 Chiapas earthquake is critical to overcome the uncertainty of the focal depths seen in the CMT analyses, and to understand the event's driving mechanism in its tectonic context.

Here we construct a seismic source model of the 2017 Chiapas earthquake with the kinematic waveform inversion method (Yagi & Fukahata, 2011) by using globally observed teleseismic *P* waveforms. Our slip model favors an intraplate normal-faulting mechanism with the peak slip at ~ 28 km depth. In this model, tensile stresses in the upper part of the subducting plate should initiate and drive the rupture, and flattening of the slab may inhibit rupture propagation northwestward of the main rupture, which are related to the subduction of the TFZ and the lateral change of the plate geometry across the TFZ.

2. Data and Method

We downloaded 34 globally observed teleseismic waveforms (vertical components) from the Incorporated Research Institutions for Seismology Data Management Center (IRISDMC;

Figure 3d). The data were selected to ensure a high signal-to-noise ratio for picking the first motion of the *P* phase clearly, as well as a good azimuthal distribution to capture the diverse radiation pattern of the waveforms. The instrumental response of each waveform was deconvolved to velocity at a sampling rate of 0.8 s. We calculated Green's functions based on the method of Kikuchi and Kanamori (1991) at 0.1 s interval, and then resampled these at 0.8 s intervals in the inversion procedure. To calculate the Haskell propagator matrix in Green's functions, we extracted a one-dimensional, near-source velocity structure from the one presented in Santoya et al. (2005) (Table S1). We considered the uncertainties of the slip model derived from the near-source velocity structures by testing the velocity structures of Rebollar et al. (1999a) (Table S2) and the CRUST1.0 model (Laske et al., 2013) (Table S3), thus confirming that the slip models were not significantly affected by the velocity models (Figure S4). This stability against the near-source velocity model is valid for an inversion adopting the teleseismic waveforms, as already mentioned in Yagi et al., 2004. We used the ak135 model (Kennett et al., 1995) to calculate the travel times, the geometrical spreading factors, and the ray parameters. A two-pole Butterworth band pass filter over the range of 0.001–0.21 Hz was applied to both the observed waveforms and the Green's functions; a broader range than that used for the CMT analysis (0.005–0.02 Hz) (Text S1) was used in order to retrieve the complicated rupture history recorded in a wide frequency range and to better separate the depth phases.

The uncertainty in Green's functions is a major source of modeling error in the kinematic waveform inversion procedure (Yagi & Fukahata, 2011), and it may lead to discrepancies among slip models for an earthquake produced by different researchers using different inversion schemes (Beresnev, 2003; Mai et al., 2016). We adopted the inversion scheme of Yagi and Fukahata (2011) to mitigate this uncertainty, by objectively determining the strength of smoothness constraints on the model parameters and the data covariance matrix including the uncertainty of Green's functions by minimizing the Akaike's Bayesian Information Criterion (ABIC) (Akaike, 1980; Yabuki & Matsu'ura, 1992). Guided by both the aftershock distribution determined by the SSN (Figure 1) and our CMT solution (Figure 2b), we assumed a fault geometry with a planar rectangle fault 145 km length and 65 km width, striking 316° and dipping 81° , to cover the possible source region. We used variants of the strike and dip to confirm that the arbitrariness of the fault geometry did not significantly affect our conclusions (Figures S2 and S3). We discretized the fault model into 5 km \times 5 km source nodes and adopted the SSN's epicentral location of 14.85°N , 94.11°W for the initial rupture point. For the initial rupture depth, we tried various depths between 8.1 and 67.4 km to determine the dominant depth favored by the slip model (Figure 3a). The slip-rate function on each source node was represented as a linear B-spline function over a duration of 32 s, calculated every 0.8 s and assuming a maximum rupture-front velocity at 3.5 km/s so as to flexibly represent the rupture evolution. The total source duration was limited to 50 s from the hypocentral time on the basis of the half-rise time determined by our CMT solution (Figure 2b).

3. Results

In Figure 3b, we show the depth distribution of seismic potency (seismic moment divided by rigidity) summed along strike for each model with the variable arrangement of initial rupture depth. The potency distributions for the models with initial-rupture depths at 8.1–47.6 km depths ("shallow models" hereafter) consistently displayed a peak at 28 km depth and similar patterns. The models with initial-rupture depths at 52.6–67.4 km ("deep models" hereafter) displayed peaks at 38–48 km depths. Figure 3c shows the fit between observed and synthetic waveforms at

selected stations (fits for all stations are shown in Figure S5). These fits generally degraded as the initial rupture depth increased, and the synthetic waveforms for the deep models do not explain the later phases just after the *P* phase in the observed waveforms, which can be recognized as the depth phases (*sP* and *pP*). The variance between the observed and synthetic waveforms increased (Figure S6), and the ABIC value for each model also increased if we compared the models sharing the equal number of model parameters. Our fault modeling, then, shows that the shallow models are preferable.

Although it is difficult to determine a preferred model among the shallow models given that the overall slip pattern was the same in all of them (Figure S1), we chose the model that assumed the initial rupture point at 18 km depth as the reference model for the following discussion, as it was consistent with the slab interface inferred by using the Slab1.0 model (Hayes et al., 2012; Figure 3a). In the reference slip model, the dominant rupture area, where slip exceeds 70% of the peak value, extends northwest from the epicenter over an area of 50 km × 30 km and the location of maximum slip (18.6 m) is 50 km northwest of the epicenter (Figures 4a and 4c). The slip vectors indicate pure normal faulting (Figure S1) in the dominant rupture area. The resultant moment release is 1.85×10^{21} Nm (M_w 8.1), slightly smaller than that of the GCMT solution (2.65×10^{21} Nm, M_w 8.2), which reflects the difference between the centroid depth of the dominant slip area in our model and the focal depth (50.2 km) of the GCMT solution. We show the spatiotemporal slip evolution in Figures 4d–4f, as the projections of the slip history along the strike and dip directions, and the snapshots of the cross section of the fault plane taken at the selected time, respectively. The rupture front propagated in both the strike and dip directions during the initial rupture process until 18 s from the hypocentral time. The rupture-front velocities for the strike and the dip directions are both estimated at ~3 km/s. The down-dip rupture was restricted to around 62 km depth (45 km down dip) and ceased at 12 s from the hypocentral time, whereas the rupture propagation along strike accelerated after 18 s, temporally exceeding 3 km/s in that direction (Figure 4d). This acceleration may reflect the onset of the main-rupture phase, which occurred between 18 and 35 s in the fault area 15–90 km along strike from the hypocenter. The rupture front of this phase is gradually propagated and extended down dip to 48 km depth (Figures 4e and 4f). The rupture front began to decelerate at ~85 km along strike at ~30 s (Figures 4d and 4f), and gradually terminated at ~50 s. Overall, the rupture evolution shows the almost unilateral migration toward northwest from the epicenter involving the down-dip propagation at the initial rupture stage, and then, the upper and lower limits of the main rupture area both gradually migrated deeper on the fault as the rupture front advanced (Figure 4f).

4. Discussions

The finite fault models constructed in this study suggest that the rupture area was centered at 28 km depth, even if we deepen the initial rupture point down to 47.6 km depth (Figures 3a and 3b). According to the slab geometry based on the Slab1.0 model (Hayes et al., 2012), the rupturing area was below the slab interface and the upper part of the subducting Cocos plate. The slip vectors indicate almost pure normal faulting (Figure S1), suggesting that the 2017 Chiapas earthquake was an intraplate, normal-faulting event, resulting from the tensile stresses oriented in the dip direction of the subducting plate. The geometry of the subducting plate around the source region is probably affected by the subduction of the TFZ in the Cocos plate (Figure 1). The dip angle of the Cocos plate gradually changes from ~20° west of the TFZ to ~40° east of the TFZ (Ponce et al., 1992; Rebollar et al., 1999a), and the seafloor bathymetry seaward of the

trench also shows a lateral variation across the TFZ (Figure 1). We infer that the tensile stress is concentrated around the source region by slab bending related to the change in dip of the Cocos plate across the TFZ. As shown in Figures 4e and 4f, the upper and lower edges of the rupture area moved deeper as the rupture front propagated northwest, and the down-dip width of the main rupture was limited to 30 km. If the slab was bending at the source region, the down-dip stress should be extensional in the upper part of the slab and compressional in the lower part (e.g., Astiz et al., 1988). This change in stress may account for the main rupture area being dominantly in the upper part of the plate, with its down-dip width and down-dip edge defined by the transition of the stress regime from extension to compression. The downward rupture propagation and the limited width of the main rupture may reflect lateral changes in the slab geometry and thermal structure (e.g., Manea & Manea, 2008) along the strike direction, and the down-dip edge of the main rupture area may correspond to the brittle-ductile transition in the oceanic lithosphere. Earthquake swarms around the epicenter (Figure 1) detected by Nishikawa and Ide (2017) may be independent evidence of slab bending around the source region, because fracturing and hydration in the plate due to bending may manifest as high seismicity rates (Nishikawa & Ide, 2015; Poli et al., 2017; Ranero et al., 2003; Shillington et al., 2015), and such a relation between earthquake swarms and subduction of a fracture zone has been documented in the Coquimbo-Illapel region of central Chile (e.g., Poli et al., 2017).

The main rupture phase extended from 15 to 90 km along strike during the period 18–35 s, characterized by a rapid acceleration at 18 s and abrupt deceleration at 30 s (Figure 4d). The abrupt deceleration at ~85 km along strike is consistent with the intersection of the fault plane with the extended axis of the TFZ. The dip angle of the plate boundary is shallower near the TFZ axis than southeast of the TFZ, where the rupture initiated and where the main rupture occurred. Although the geometry of the plate around the source region is unclear in detail, the abrupt deceleration of the rupture may indicate that the changes in plate geometry along the strike direction of the fault plane is a geometric barrier (e.g., Aki, 1979; Das & Aki, 1977) inhibiting rupture propagation across the TFZ.

5. Conclusion

We carried out a detailed analysis of the seismic source process of the M_w 8.1 2017 Chiapas earthquake by kinematic waveform inversion of globally observed teleseismic waveforms. The model presented in this study suggests that the rupture process was driven by down-dip extensional stresses caused by slab bending in shallow parts of the subducting Cocos plate and that a lateral change in the slab geometry along the strike direction restricted rupture propagation across the TFZ. The possibility of steeply dipping normal faulting in the shallow slab, landwards of the trench, due to slab bending is a fresh view of the subduction zone process in southern Mexico that may be critical in assessing future tsunami risk along this coast.

Acknowledgments

We thank Carlos Villafuerte, Kohtaro Ujiie, Suguru Endo, Takeshi Mikumo, Tomoaki Nishikawa, and Vladimir Kostoglodov for their valuable comments and suggestions. This work was supported by a Grant-in-aid for a Japan Society for the Promotion of Science (JSPS) Research Fellow (JP16J00298), JSPS Grants-in-aid for Scientific Research (JP16K05529, JP16H01842, and JP16K05539), and JSPS KAKENHI Grant Number JP16H06477 in Scientific Research on Innovative Areas “Science of Slow Earthquakes”. Figures were generated with

matplotlib version 2.0.2 (<http://doi.org/10.5281/zenodo.592536>) (Hunter, 2007) and ObsPy version 1.0.3 (<http://doi.org/10.5281/zenodo.165134>) (Beyreuther et al., 2010). The IRISDMC provided access to the waveforms and related metadata from the seismic networks of II: IRIS/IDA Seismic Network (<http://dx.doi.org/doi:10.7914/SN/II/>) and IU: Global Seismograph Network (GSN - IRIS/USGS) (GSN; <http://dx.doi.org/doi:10.7914/SN/IU>). Hypocentral information for seismicity along the Mexico subduction zone was provided by the SSN UNAM (<http://www.ssn.unam.mx>). All the data and materials to derive the conclusions of this study are archived on Github (<https://github.com/rokuwaki>).

References

- Akaike, H. (1980). Likelihood and the Bayes procedure. *Trabajos de Estadística Y de Investigación Operativa*, 31(1), 143–166. <https://doi.org/10.1007/BF02888350>
- Aki, K. (1979). Characterization of barriers on an earthquake fault. *Journal of Geophysical Research*, 84(B11), 6140. <https://doi.org/10.1029/JB084iB11p06140>
- Astiz, L., Lay, T., & Kanamori, H. (1988). Large intermediate-depth earthquakes and the subduction process. *Physics of the Earth and Planetary Interiors*, 53(1–2), 80–166. [https://doi.org/10.1016/0031-9201\(88\)90138-0](https://doi.org/10.1016/0031-9201(88)90138-0)
- Beresnev, I. A. (2003). Uncertainties in Finite-Fault Slip Inversions: To What Extent to Believe? (A Critical Review). *Bulletin of the Seismological Society of America*, 93(6), 2445–2458. <https://doi.org/10.1785/0120020225>
- Beyreuther, M., Barsch, R., Krischer, L., Megies, T., Behr, Y., & Wassermann, J. (2010). ObsPy: A Python Toolbox for Seismology. *Seismological Research Letters*, 81(3), 530–533. <https://doi.org/10.1785/gssrl.81.3.530>
- Bravo, H., Rebollar, C. J., Uribe, A., & Jimenez, O. (2004). Geometry and state of stress of the Wadati-benioff zone in the Gulf of Tehuantepec, Mexico. *Journal of Geophysical Research B: Solid Earth*, 109(4), 1–14. <https://doi.org/10.1029/2003JB002854>
- Christensen, D. H., & Ruff, L. J. (1985). Analysis of the Trade-Off Between Hypocentral Depth and Source Time Function. *Bulletin of the Seismological Society of America*, 75(6), 1637–1656.
- Das, S., & Aki, K. (1977). Fault plane with barriers: A versatile earthquake model. *Journal of Geophysical Research*, 82(36), 5658–5670. <https://doi.org/10.1029/JB082i036p05658>
- DeMets, C., Gordon, R. G., & Argus, D. F. (2010). Geologically current plate motions. *Geophysical Journal International*, 181(1), 1–80. <https://doi.org/10.1111/j.1365-246X.2009.04491.x>
- Ekström, G., Nettles, M., & Dziewoński, A. M. (2012). The global CMT project 2004–2010: Centroid-moment tensors for 13,017 earthquakes. *Physics of the Earth and Planetary Interiors*, 200–201, 1–9. <https://doi.org/10.1016/j.pepi.2012.04.002>
- Fujita, K., & Kanamori, H. (1981). Double seismic zones and stresses of intermediate depth earthquakes. *Geophysical Journal International*, 66(1), 131–156. <https://doi.org/10.1111/j.1365-246X.1981.tb05950.x>

- 276 Hayes, G. P., Wald, D. J., & Johnson, R. L. (2012). Slab1.0: A three-dimensional model of
277 global subduction zone geometries. *Journal of Geophysical Research: Solid Earth*, 117(B1), n/a-
278 n/a. <https://doi.org/10.1029/2011JB008524>
- 279 Hunter, J. D. (2007). Matplotlib: A 2D Graphics Environment. *Computing in Science &*
280 *Engineering*, 9(3), 90–95. <https://doi.org/10.1109/MCSE.2007.55>
- 281 Isacks, B., Oliver, J., & Sykes, L. R. (1968). Seismology and the new global tectonics. *Journal of*
282 *Geophysical Research*, 73(18), 5855–5899. <https://doi.org/10.1029/JB073i018p05855>
- 283 Kennett, B. L. N., Engdahl, E. R., & Buland, R. (1995). Constraints on seismic velocities in the
284 Earth from traveltimes. *Geophysical Journal International*, 122(1), 108–124.
285 <https://doi.org/10.1111/j.1365-246X.1995.tb03540.x>
- 286 Kikuchi, M., & Kanamori, H. (1991). Inversion of complex body waves—III. *Bulletin of the*
287 *Seismological Society of America*, 81(6), 2335–2350.
- 288 Laske, G., Masters, G., Ma, Z., & Pasyanos, M. (2013). Update on CRUST1. 0—A 1-degree
289 global model of Earth's crust. *EGU General Assembly*, 15, 2658.
- 290 LeFevre, L. V., & McNally, K. C. (1985). Stress distribution and subduction of aseismic ridges
291 in the Middle America Subduction Zone. *Journal of Geophysical Research: Solid Earth*, 90(B6),
292 4495–4510. <https://doi.org/10.1029/JB090iB06p04495>
- 293 Lemoine, A., Madariaga, R., & Campos, J. (2002). Slab-pull and slab-push earthquakes in the
294 Mexican, Chilean and Peruvian subduction zones. *Physics of the Earth and Planetary Interiors*,
295 132(1–3), 157–175. [https://doi.org/10.1016/S0031-9201\(02\)00050-X](https://doi.org/10.1016/S0031-9201(02)00050-X)
- 296 Mai, P. M., Schorlemmer, D., Page, M., Ampuero, J., Asano, K., Causse, M., ... Zielke, O.
297 (2016). The Earthquake-Source Inversion Validation (SIV) Project. *Seismological Research*
298 *Letters*, 87(3), 690–708. <https://doi.org/10.1785/0220150231>
- 299 Manea, M., & Manea, V. C. (2008). On the origin of El Chichón volcano and subduction of
300 Tehuantepec Ridge: A geodynamical perspective. *Journal of Volcanology and Geothermal*
301 *Research*, 175(4), 459–471. <https://doi.org/10.1016/j.jvolgeores.2008.02.028>
- 302 Manea, M., Manea, V. C., & Kostoglodov, V. (2003). Sediment fill in the Middle America
303 Trench inferred from gravity anomalies. *Geofisica Internacional*, 42(4), 603–612.
- 304 Menard, H., & Fisher, R. L. (1958). Clipperton fracture zone in the northeastern equatorial
305 Pacific. *The Journal of Geology*, 66(3), 239–253. <https://doi.org/10.2307/30080925>
- 306 Mikumo, T., Santoyo, M. A., & Singh, S. K. (2000). Dynamic rupture and stress change in a
307 normal faulting earthquake in the subducting Cocos plate. *Geophysical Journal International*,
308 140(3), 611–620. <https://doi.org/10.1046/j.1365-246X.2000.00055.x>
- 309 Mikumo, T., Singh, S. K., & Santoyo, M. A. (1999). A possible stress interaction between large
310 thrust and normal faulting earthquakes in the Mexican subduction zone. *Bulletin of the*
311 *Seismological Society of America*, 89(6), 1418–1427.
- 312 Mikumo, T., Yagi, Y., Singh, S. K., & Santoyo, M. A. (2002). Coseismic and postseismic stress
313 changes in a subducting plate: Possible stress interactions between large interplate thrust and
314 intraplate normal-faulting earthquakes. *Journal of Geophysical Research: Solid Earth*, 107(B1),
315 ESE 5-1-ESE 5-12. <https://doi.org/10.1029/2001JB000446>

- 316 Nishikawa, T., & Ide, S. (2017). Detection of earthquake swarms at subduction zones globally:
 317 Insights into tectonic controls on swarm activity. *Journal of Geophysical Research: Solid Earth*,
 318 122(7), 5325–5343. <https://doi.org/10.1002/2017JB014188>
- 319 Nishikawa, T., & Ide, S. (2015). Background seismicity rate at subduction zones linked to slab-
 320 bending-related hydration. *Geophysical Research Letters*, 42(17), 7081–7089.
 321 <https://doi.org/10.1002/2015GL064578>
- 322 Pardo, M., & Suárez, G. (1995). Shape of the subducted Rivera and Cocos plates in southern
 323 Mexico: Seismic and tectonic implications. *Journal of Geophysical Research: Solid Earth*,
 324 100(B7), 12357–12373. <https://doi.org/10.1029/95JB00919>
- 325 Poli, P., Jeria, A. M., & Ruiz, S. (2017). The M_w 8.3 Illapel earthquake (Chile): Preseismic and
 326 postseismic activity associated with hydrated slab structures. *Geology*, 45(3), 247–250.
 327 <https://doi.org/10.1130/G38522.1>
- 328 Ponce, L., Gaulon, R., Suárez, G., & Lomas, E. (1992). Geometry and state of stress of the
 329 downgoing Cocos Plate in the Isthmus of Tehuantepec, Mexico. *Geophysical Research Letters*,
 330 19(8), 773–776. <https://doi.org/10.1029/92GL00437>
- 331 Ramírez-Herrera, M. T., Kostoglodov, V., & Urrutia-Fucugauchi, J. (2011). Overview of recent
 332 coastal tectonic deformation in the Mexican subduction zone. *Pure and Applied Geophysics*,
 333 168(8–9), 1415–1433. <https://doi.org/10.1007/s0024-010-0205-y>
- 334 Ranero, C. R., Phipps Morgan, J., McIntosh, K., & Reichert, C. (2003). Bending-related faulting
 335 and mantle serpentinization at the Middle America trench. *Nature*, 425(6956), 367–373.
 336 <https://doi.org/10.1038/nature01961>
- 337 Rebollar, C. J., Espíndola, V. H., Uribe, A., Mendoza, A., & Pérez-Vertti, A. (1999a).
 338 Distributions of stresses and geometry of the Wadati-Benioff zone under Chiapas, Mexico.
 339 *Geofísica Internacional*, 38(2), 95–106.
- 340 Rebollar, C. J., Quintanar, L., Yamamoto, J., & Uribe, A. (1999b). Source process of the
 341 Chiapas, Mexico, intermediate-depth earthquake (M_w = 7.2) of 21 October 1995. *Bulletin of the*
 342 *Seismological Society of America*, 89(2), 348–358.
- 343 Santoyo, M. A., Singh, S. K., & Mikumo, T. (2005). Source process and stress change associated
 344 with the 11 January, 1997 (M_w=7.1) Michoacán, Mexico, inslab earthquake. *Geofísica*
 345 *Internacional*, 44(4), 317–330.
- 346 Shillington, D. J., Bécel, A., Nedimović, M. R., Kuehn, H., Webb, S. C., Abers, G. A., ...
 347 Mattei-Salicrup, G. A. (2015). Link between plate fabric, hydration and subduction zone
 348 seismicity in Alaska. *Nature Geoscience*, 8(12), 961–964. <https://doi.org/10.1038/ngeo2586>
- 349 Singh, S. K., Astiz, L., & Havskov, J. (1981). Seismic gaps and recurrence periods of large
 350 earthquakes along the Mexican subduction zone: A reexamination. *Bulletin of the Seismological*
 351 *Society of America*, 71(3), 827–843. Retrieved from
 352 <http://www.bssaonline.org/content/71/3/827.abstract>
- 353 Singh, S. K., Suárez, G., & Domínguez, T. (1985). The Oaxaca, Mexico, earthquake of 1931:
 354 lithospheric normal faulting in the subducted Cocos plate. *Nature*, 317(6032), 56–58.
 355 <https://doi.org/10.1038/317056a0>

- Spence, W. (1986). The 1977 Sumba earthquake series: Evidence for Slab pull force acting at a subduction zone. *Journal of Geophysical Research: Solid Earth*, 91(B7), 7225–7239. <https://doi.org/10.1029/JB091iB07p07225>
- SSN UNAM Special Report. (2017). Reporte Especial Sismo de Tehuantepec (2017-09-07 23:49 M8.2). Retrieved September 21, 2017, from http://www.ssn.unam.mx/sismicidad/reportes-especiales/2017/SSNMX_rep_esp_20170907_Tehuantepec_M82.pdf
- Vallée, M., Charléty, J., Ferreira, A. M. G., Delouis, B., & Vergoz, J. (2011). SCARDEC: a new technique for the rapid determination of seismic moment magnitude, focal mechanism and source time functions for large earthquakes using body-wave deconvolution. *Geophysical Journal International*, 184(1), 338–358. <https://doi.org/10.1111/j.1365-246X.2010.04836.x>
- Vallée, M., & Douet, V. (2016). A new database of source time functions (STFs) extracted from the SCARDEC method. *Physics of the Earth and Planetary Interiors*, 257, 149–157. <https://doi.org/10.1016/j.pepi.2016.05.012>
- Yabuki, T., & Matsu'ura, M. (1992). Geodetic data inversion using a Bayesian information criterion for spatial distribution of fault slip. *Geophysical Journal International*, 109, 363–375.
- Yagi, Y., & Fukahata, Y. (2011). Introduction of uncertainty of Green's function into waveform inversion for seismic source processes. *Geophysical Journal International*, 186(2), 711–720. <https://doi.org/10.1111/j.1365-246X.2011.05043.x>
- Yagi, Y., Mikumo, T., Pacheco, J., & Reyes, G. (2004). Source rupture process of the Tecomán, Colima, Mexico earthquake of 22 January 2003, determined by joint inversion of teleseismic body-wave and near-source data. *Bulletin of the Seismological Society of America*, 94(5), 1795–1807. <https://doi.org/10.1785/012003095>

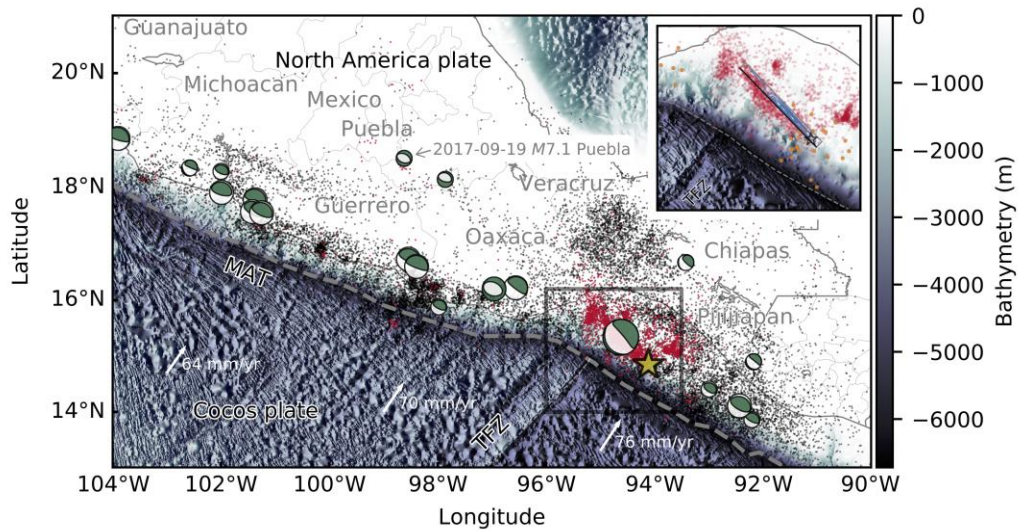


Figure 1. Map overview around the source region of the 2017 Chiapas Mexico earthquake. Star denotes the mainshock epicenter, and red and black dots are the epicenters of two-week-aftershock ($M \geq 3$), and the seismicity ($M \geq 4$) between January 1, 1990 to September 7, 2017, respectively, all determined by the SSN. Beach balls show the GCMT solutions of the $M_w \geq 7$ earthquakes occurred in 1978–2017 (Ekström et al., 2012), including the $M_{7.1}$ 2017 Puebla, Mexico earthquake. Dashed line shows the MAT, and thin dashed line represents the TFZ drawn with the coordinates given by the General Bathymetric Chart of the Oceans (GEBCO) Undersea Fracture Names Gazetteer (<https://www.ngdc.noaa.gov/gazetteer/>). Arrows indicate the motions of the Cocos plate relative to the fixed Pacific plate employing the MORVEL model (DeMets et al., 2010), and the coordinates of them are calculated with Plate Motion Calculator provided by UNAVCO (<https://www.unavco.org>). Rectangle delimits the inset map shown on upper right corner. Background bathymetry is derived from the GEBCO_2014 Grid, version 20150318, <http://www.gebco.net>. Inset map shows the cumulative slip distribution of the model presented in Figure 4, with slip contours every 3.0 m. Orange dots represent the locations of the earthquake swarms (Nishikawa & Ide, 2017). Gray rectangle in the inset map delimits the fault plane along with the fault top as black line.

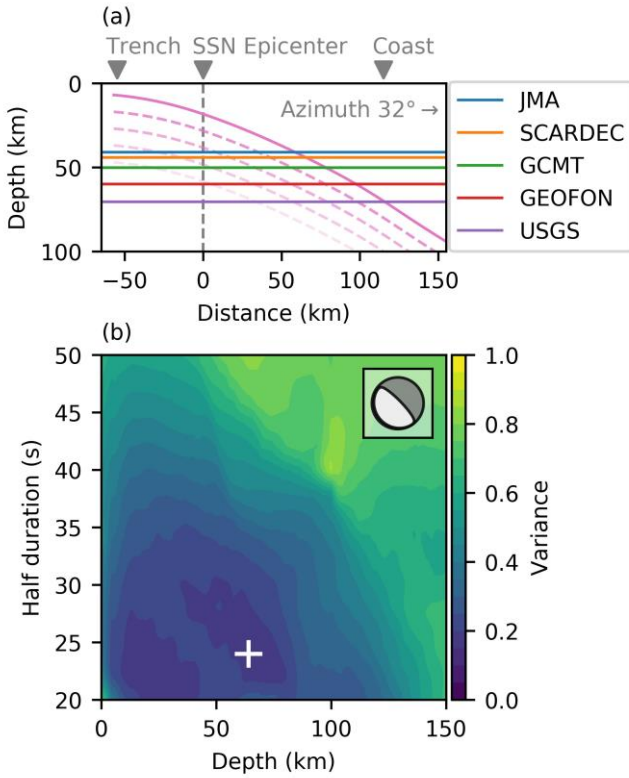


Figure 2. Cross section of the source area and the CMT solutions. (a) Cross section of the source region, with abscissa for the distance from the epicenter determined by the SSN. Pink curve shows the Slab1.0 model (Hayes et al., 2012), along with the isodepths every 10 km as dashed pink curves. Colored horizontal lines represent the focal depths determined by the JMA, SCARDEC, GCMT, GEOFON, and USGS. (b) Variance distribution of the CMT analysis in this study. Background color shows the variance of the synthetic and observed waveforms. Cross marker denotes the variance minimum at 64.0 km depth and 24 s half duration. Inset at upper right corner is the focal mechanism determined by our CMT analysis.

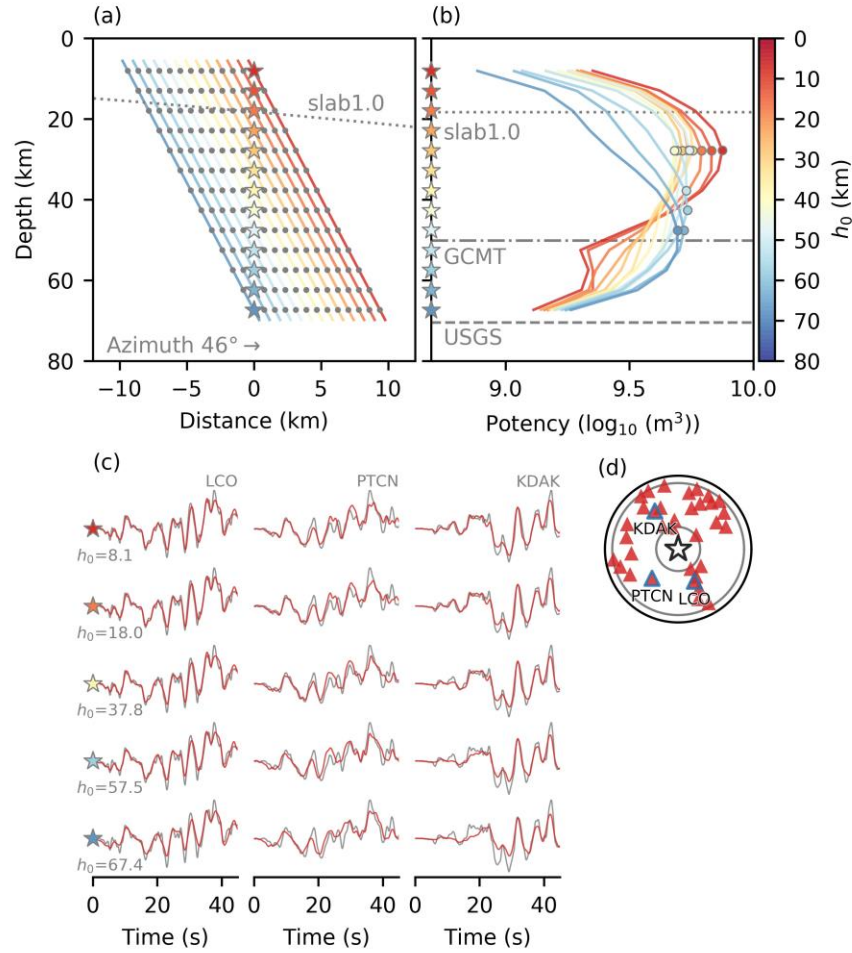


Figure 3. Model settings and the results. (a) Cross section of the fault geometries. Each line shows the fault plane, along with the initial rupture point and the source nodes denoted as star and dots, respectively. Dotted curve represents the Slab1.0 model (Hayes et al., 2012). (b) Potency distribution along depth summed along strike for each slip model. Star denotes the initial rupture depth (h_0) for each model. Peak location of the potency distribution for each model is denoted as colored dot. Horizontal lines are the focal depths determined by the GCMT and the USGS, and the mean depth of the slab1.0 model (Hayes et al., 2012). (c) Waveform fittings at LCO, PTCN, and KDAK stations. Location of each station is denoted in Figure 3d. Red and gray lines represent the normalized amplitudes of the synthetic and observed waveforms, respectively. Each trace is aligned with the first arrivals of P-phase. (d) Station distribution in azimuthal equidistant projection, used through the CMT analysis and the finite fault modeling in this study. Star and triangles denote the epicenter and the station locations, respectively. Gray lines represent the epicentral distances of 30° and 90° .

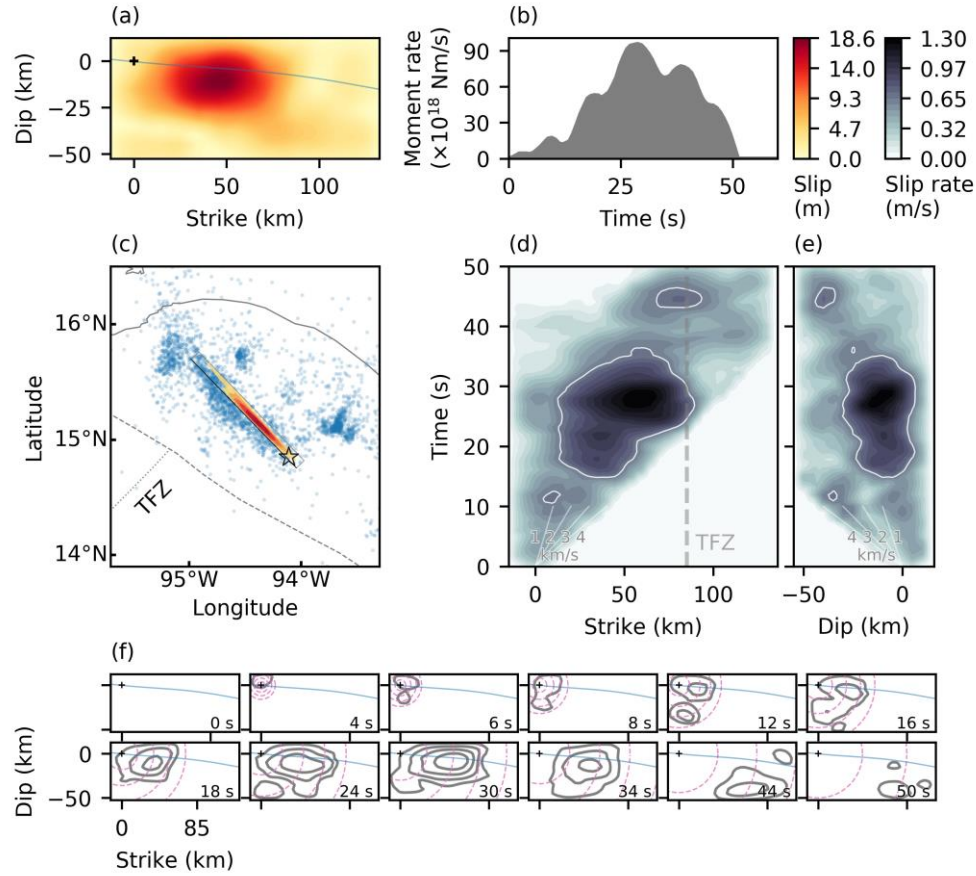


Figure 4. Summary of the slip model with the initial rupture depth of 18 km. (a) Cross section of the cumulative slip distribution. Background color shows the slip amplitude. Cross marker represents the initial rupture point. (b) Graph shows the moment-rate function. (c) Map view of the accumulated slip distribution. Color contour denotes every 3.0 m slip. Rectangle delimits the fault plane along with the fault top as black line. Star and blue dots are the epicenters of the mainshock and the two-week-aftershock ($M \geq 3$) determined by the SSN. Slip evolutions projected along (d) strike and (e) dip directions of the fault plane. Background color represents the amplitude of the slip rate. White contour denotes the slip rate at 0.65 m/s (50% of maximum slip rate). Dashed line represents the expected location of the TFZ extended from the MAT. Reference rupture speeds at 1, 2, 3, and 4 km/s are denoted as white lines. (d) Selected snapshots of the slip model. Time where the snapshot is taken is on right bottom corner of each panel. Gray contour denotes the slip rate every 0.26 m/s. Cross marker shows the initial rupture point, and blue curve represents the Slab1.0 model (Hayes et al., 2012). Pink dashed lines are the reference rupture speeds that constantly expand in a circle at 1, 2, 3, and 4 km/s.